Pergamon

Int. J. Solids Structures Vol. 35, No. 21, pp. 2821–2842, 1998

0020–7683/98 $19.00 + .00

PII: S0020–7683(97)00279–5

LIMIT STRESS CONDITIONS FOR WEAKLY BONDED FIBER COMPOSITES SUBJECT TO TRANSVERSE BIAXIAL TENSILE LOADING

Z.-Z. DU* and F. W. ZOK
Materials Department, University of California, Santa Barbara, California 93106, U.S.A.

(*Received* 1 *April* 1997; *in revised form* 1 *September* 1997)

Abstract—This paper focuses on the limit stress conditions of metal matrix composites reinforced with weakly-bonded continuous fibers subject to general biaxial tensile loading normal to the fiber direction. The study is performed using unit cell models, with the fibers being treated as either perfectly rigid or perfectly compliant. The cells are first analyzed using finite element methods (FEM) and the results used to construct yield surfaces in stress space. A simpler analytical model based on net-section yielding is also developed and the results compared with the ones obtained by FEM. Though the latter approach provides a reasonable first order estimate of the limited stress, it generally underestimates the values obtained from the FEM calculations: a result of stress gradients acting along the failure plane. The effects of stress gradients are incorporated into the net-section yielding model through an analytical solution based upon the slip line field around a circular hole. This approach yields analytical predictions which are generally in very good agreement with the FEM results. © 1998 Elsevier Science Ltd. All rights reserved.

1. INTRODUCTION

The plastic flow and creep properties of continuous fiber-reinforced metal matrix composites (MMCs) exhibit varying degrees of anisotropy, depending on the properties of the constituents (matrix, fibers and interfaces) and the fiber architecture. In unidirectionally reinforced materials, the properties measured along the axis of the fibers are usually dominated by the fibers and are superior to those of the matrix alloy alone (Jansson *et al.*, 1991; Weber, *et al.*, 1994). In contrast, under transverse or shear loading, the properties are matrix-dominated. Even in the best of circumstances, wherein the fibers are well-bonded to the matrix, the contributions from the fibers are relatively small except at very high fiber volume fractions ($\geqslant 50\%$). This type of behavior is exemplified by the Al/Al_2O_3 and Al/B systems (Jansson and Leckie, 1992). In systems comprised of SiC fibers in Ti alloys, the interfaces between the fibers and matrix are weak because of the presence of C coatings. In these systems, the transverse and shear properties fall below those of the matrix alone (Jansson *et al.*, 1991; Jansson and Leckie, 1994; Weber *et al.*, 1995). Typically, the ratio of axial to transverse tensile strengths in Ti/SiC composites at ambient temperature is ~ 4. At elevated temperatures, the matrix strength decreases, causing an increase in the anisotropy of the composite strength (Weber *et al.*, 1995). The strength anisotropy has important implications regarding the design of structural components using MMCs, particularly under conditions of multiaxial stress. Indeed, the anisotropy represents one of the most severe drawbacks associated with this class of composite and may limit the use of MMCs in structural applications.

The transverse flow and creep properties of well-bonded fiber-reinforced MMCs under uniaxial loading have been studied by numerous investigators through calculations based on finite element methods (FEM) (Teply and Dvorak, 1988; Brockenbrough and Suresh, 1990; Brockenbrough *et al.*, 1991; Nakamura and Suresh, 1993; Zahl *et al.*, 1994; Du and McMeeking, 1994). A relatively comprehensive series of numerical results is documented in Zahl *et al.* (1994). One of the key results emanating from these studies is that, at sufficiently large strains, the ratio of the composite flow stress, $\sigma_c(\varepsilon)$, to that of the matrix, $\sigma_m(\varepsilon)$, reaches a constant (steady-state) value, dependent only of the fiber volume fraction,

* Now at Hibbitt, Karlsson and Sorensen, Inc., 1080 Main St., Pawtucket, RI 02860, U.S.A.

f, and the hardening characteristics of the matrix. The transient response preceding this steady-state persists for strains that are typically in the range of $\sim(1\text{–}5)\varepsilon_0$, with ε_0 being the yield strain of the matrix. For modest values of $f(<0.35)$, the steady state strength ratio is given approximately by $\sigma_c(\varepsilon)/\sigma_m(\varepsilon) \approx 2/\sqrt{3} \approx 1.15$; the main role of the fibers is to constrain the matrix from contracting along the fiber direction, leading to conditions of plane strain. Substantial elevations in strength are only obtained for high fiber volume fractions ($f > 0.5$).

The influence of thermal residual stress on the transverse tensile response of well-bonded systems has been examined also (Nakamura and Suresh, 1993, Böhm and Rammerstorfer, 1991). A general result is that the steady-state strength ratio, $\sigma_c(\varepsilon)/\sigma_m(\varepsilon)$, is independent of the thermal stress; the thermal stress only influences the transient response. The magnitude of the transient effect depends on the thermal misfit strain and the flow and hardening characteristics of the matrix.

Limited numerical studies have been conducted for materials with weak interfaces, subject to uniaxial tensile loading transverse to the fibers (Nimmer *et al.*, 1991; Gunawardena *et al.*, 1993). In these cases, the composite strength is less than the yield strength of the matrix alone. The effects of thermal residual stress and frictional sliding along the fiber/matrix interfaces have been considered also. In cases where the matrix thermal expansion coefficient, α_m, exceeds that of the fibers, α_f (a characteristic of most MMCs), the interface experiences a residual normal compression following cooling from the processing temperature. Consequently, the remote stress required to separate the interface is higher than that in a residual stress-free composite. Comparisons of the FEM calculations with experimental data on a Ti/SiC composite indicate that the condition for interface separation is one in which the local normal stress across the interface becomes positive (Gunawardena *et al.*, 1993). This results suggests that the interfaces have essentially zero normal strength and the fibers are held in place by the residual compression stress acting across the interface. Clearly the residual stress alters the initial transient part of the stress–strain response, but, as in the case of well-bonded systems, the steady-state plastic response is unaffected. Frictional sliding at the interface appears to play only a minor role in the flow response. FEM calculations have been conducted using a Coulomb friction law to characterize the sliding resistance of the interface and indicate that the flow response of the composite remains essentially unchanged for friction coefficients in the range, $\mu = 0$ to 1 (Gunawardena *et al.*, 1993).

The models of the flow response of continuous fiber composites have been limited to uniaxial loading. In practice, however, these materials are expected to be subjected locally to multiaxial stress states, even in components that are nominally loaded principally in just one direction. The multiaxiality arises because of stress concentrations, such as those present at regions where the components are joined to monolithic alloys. To motivate the current work, one specific example is cited. Ti/SiC composites are being considered for use in actuator piston rods for aircraft engines. The rods are comprised essentially of a hollow thin-walled tube of unidirectionally reinforced Ti/SiC. The tubes are clad on both the inside and the outside with layers of monolithic Ti, and the ends of the tubes are attached to monolithic Ti end fittings of rather complex shape. Though the loads are applied principally along the tube axis, there is some degree of bending, which causes tensile hoop and radial stresses near the ends of the tube (Du, *et al.*, 1996). An understanding of the effect of this triaxiality on the flow and fracture response of Ti/SiC composites is needed in order to produce reliable designs.

The current work represents an initial attempt at developing models and solutions for plastic failure of weakly-bonded fiber reinforced MMCs subject to multiaxial stress states. In this paper, the scope is restricted to biaxial tensile loading transverse to the fiber direction in unidirectional materials. Fully multiaxial (3D) conditions have yet to be addressed. The emphasis is on the plastic limit stress conditions; no consideration is given to other failure modes. As such, the predicted failure stresses are expected to be upper bounds to the stresses that composites may support in actual components. The effects of the fiber volume fraction, the spatial arrangement of the fibers, and the direction of loading in relation to the fiber arrangement are considered. The results are based on both FEM and analytical calculations.

The results are used to construct the yield surfaces using stress parameters that characterize the mean and deviatoric components of the stress state.

2. CELL MODELS AND CONSTITUENT PROPERTIES

The flow properties of the composites are examined through the analysis of unit cell models. For this purpose, the fibers are assumed to be distributed on a periodic array and the loading directions, relative to the directions characterizing the symmetry of the array, are prescribed. The periodic idealization is a good representation of most Ti/SiC composites wherein the fibers are distributed uniformly through the matrix; it may be a less accurate representation of composites produced by melt infiltration because of the more random fiber distribution.

The present study focuses on unit cells derived from the hexagonal and square fiber arrangements. Two typical unit cells and finite element grids for a fiber volume fraction, $f = 0.35$, are shown in Fig. 1. Similar cells were constructed for fiber volume fractions of $f = 0.25$ and 0.50. This range of volume fractions brackets the range found in all Ti/SiC composites of commercial interest. Uniaxial tension was simulated by imposing uniform tensile displacements on one pair of cell faces and calculating the corresponding average surface traction, either σ_{xx} or σ_{yy}. The faces normal to the applied stress were required to remain planar in order to maintain compatibility with adjacent cells. Moreover, plane strain conditions were imposed in the z-direction (along the fiber axis). For the square array,

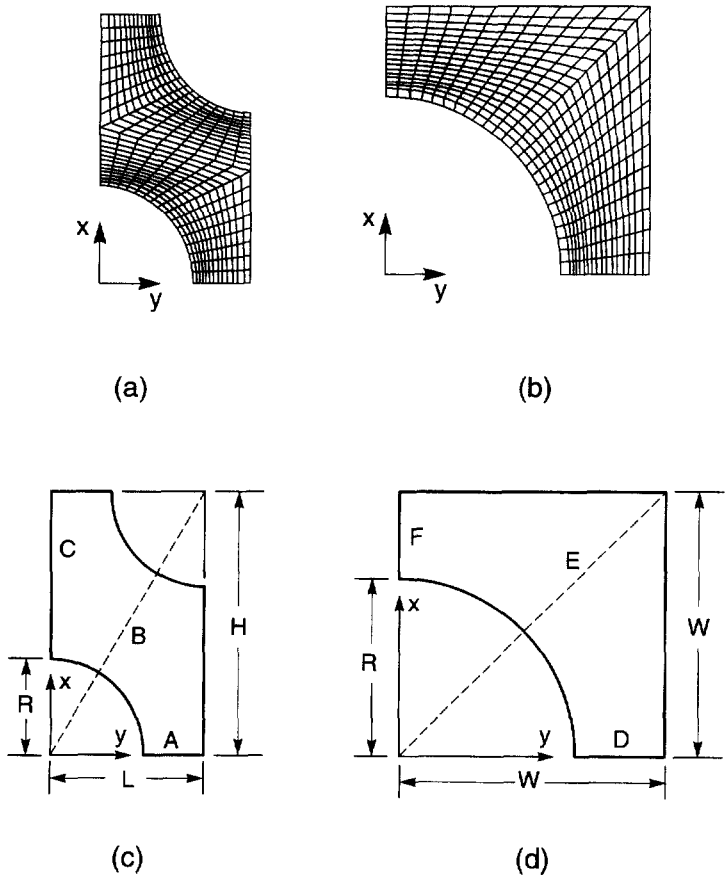

Fig. 1. Typical finite element grids for cells with a fiber volume fraction, $f = 0.35$: (a) square arrangement, (b) hexagonal arrangement. In (a), the load is applied parallel to the close-packed direction (either the x- or y-directions). In (b), the load is applied either parallel (y) or perpendicular (x) to the close packed direction. (c) and (d) show cell dimensions and the potential planes along which plastic failure can occur.

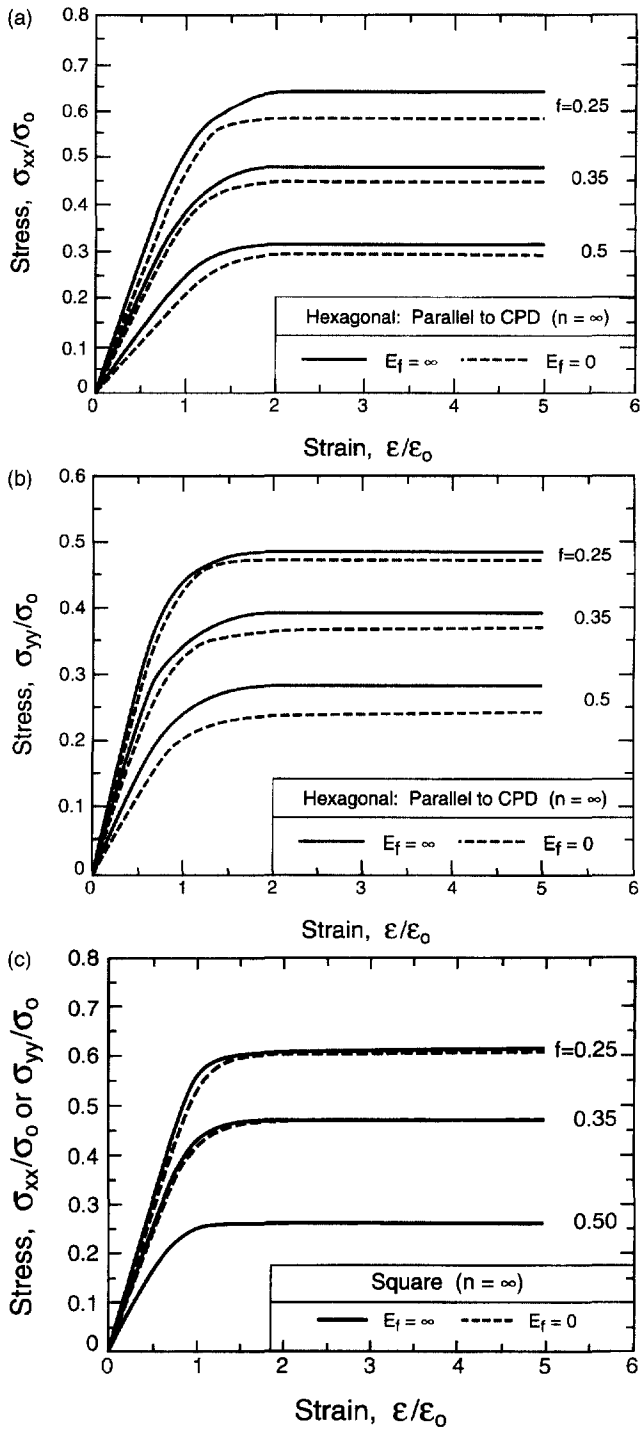

Fig. 2. Stress–strain curves for composites with (a) a hexagonal array of fibers loaded normal to the CPD, (b) a hexagonal array of fibers loaded parallel to the CPD and (c) a square fiber array. The solid lines represent the results for perfectly rigid fibers and the dashed lines are for perfectly compliant fibers.

tensile loading on either pair of cell faces yields identical results because of the symmetry of the cell. In contrast, for the hexagonal array, the two loading configurations yield different results since the axes that characterize the symmetry of the cell do not coincide with the principal loading axes. The two loading configurations are subsequently distinguished from one another by the directions of loading in relation to the closed-packed

direction (CPD) of the fibers; in Fig. 1(b), loading along the x-axis is normal to the CPD whereas loading along the y-axis is parallel to the CPD.

Biaxial loading was simulated by prescribing the boundary displacements on the two orthogonal directions to be proportional to one another and subsequently calculating the limiting values of the two stress components, σ_{xx} and σ_{yy}. The ratio of displacements was varied in order to obtain a range of stress ratios, σ_{xx}/σ_{yy}.

Most of the calculations were based on the assumption that the matrix is elastic, perfectly-plastic, with Young's modulus, E_m, Poisson's ratio, ν, and yield stress, σ_0 and yield strain, $\varepsilon_0 = \sigma_0/E_m$. In some cases, the matrix response was assumed to follow the Ramberg–Osgood flow law. For uniaxial tensile loading, this law is given by

$$\varepsilon/\varepsilon_0 = \sigma/\sigma_0 + \alpha(\sigma/\sigma_0)^n \tag{1}$$

where σ and ε are the axial stress and strain, respectively; α is a numerical coefficient, taken to be 3/7; n is the hardening exponent; σ_0 is a reference stress and ε_0 is the corresponding reference strain. Equation (1) was generalized to multiaxial stress states using small strain J_2 flow theory. For deformations much greater than the elastic ones, the stresses and strains at a material point increase in proportion to each other under proportional loading and the resulting solution is equivalent to that for J_2 deformation theory. The resulting strain field is then the same as the strain rate field for a creeping material with a power-law creep exponent of n. This equivalence implies that the solutions obtained for power-hardening are also applicable to power-law creep (Odqvist, 1966).

The fibers are treated in one of two ways: either perfectly rigid (with a Young's modulus, $E_f = \infty$) or perfectly compliant ($E_f = 0$). The latter assumption is equivalent to treating the fibers as holes. For cases where the fibers are rigid, the interface is assumed to have zero normal tensile strength.

In the light of the introductory comments regarding the absence of any effects of thermal stress on the limit stress conditions, the thermal stresses are not incorporated into the analysis. Despite this simplification, the present results for the transient response are expected to be applicable at high temperatures and low stresses, wherein the thermal stresses have adequate opportunity to relax through matrix creep. In contrast, the predicted transient at low temperatures may be subject to some uncertainty, depending on the magnitude of the thermal misfit strain.

Finite element calculations were performed using a commercial code, ABAQUS (1994), on a Convex mainframe. The matrix was discretized using isoparametric second-order hybrid elements with reduced integration in order to avoid problems of mesh-locking associated with incompressible deformation. For the cases where the fibers were perfectly rigid, interface elements were introduced to simulate the contact between the matrix and the fibers.

The cells were also analyzed using an analytical approach based on net-section yielding. For this purpose, the potential planes along which yielding can occur were first identified from the FEM results. Figures 1(c) and (d) show schematics of the approximate locations of these planes within the unit cells. For the hexagonal array, three such planes exist, denoted by A, B and C. Analogous planes exist for the square array, denoted D, E and F, though only two of them are unique (D and E). The average normal and shear stresses acting on each of these planes were then calculated in terms of the applied stresses assuming that the stresses are distributed uniformly along these planes. Finally, the local stresses were combined with the Mises yield criterion for plane strain conditions in order to obtain the limiting values of the remote stress components. This approach generally leads to conservative estimates of the limit stress; stress gradients along the expected failure planes cause an elevation in the limit stress. This elevation, in turn, can trigger plastic failure along other planes.

The effects of the stress gradients have been incorporated explicitly into the net-section yielding model using the slip-line solution for yielding ahead of a circular notch. The same result is obtained by considering the expansion of a thick-walled circular cylinder subject

to uniform biaxial tension. It will be demonstrated that the results predicted by the modified version of this model are generally in excellent agreement with the FEM results. This approach is described in further detail in Sections 3 and 4.

3. FEM RESULTS

3.1. *Uniaxial tension*

Figure 2(a) shows the transverse stress–strain curves for composites with three different fiber volume fractions in a hexagonal array, with the load applied parallel to the CPD. The solid and dashed lines are the results obtained for composites with rigid and perfectly compliant fibers, respectively. The corresponding results for the hexagonal array loaded normal to the CPD and the square array are given in Figs 2(b) and (c), respectively. For the hexagonal arrays, the limiting strength values are only slightly higher for composites containing rigid fibers than for those containing perfectly compliant fibers (by $\sim$2–14%), whereas for the square arrangements they are essentially independent of the fiber modulus.

A summary of the uniaxial limit strengths is presented in Fig. 3. The results indicate that the strengths decrease approximately linearly with increasing fiber volume fraction and reach values of $\sim$(0.2–0.3) at a volume fraction, $f = 0.5$. For the hexagonal arrays, the limit strengths are higher when the load is applied normal to the CPD than when it is applied parallel to the CPD. This trend is contrary to the one observed for composites with strongly bonded interfaces, wherein the transverse strength is found to be nearly independent of the loading direction (Zahl *et al.*, 1994).

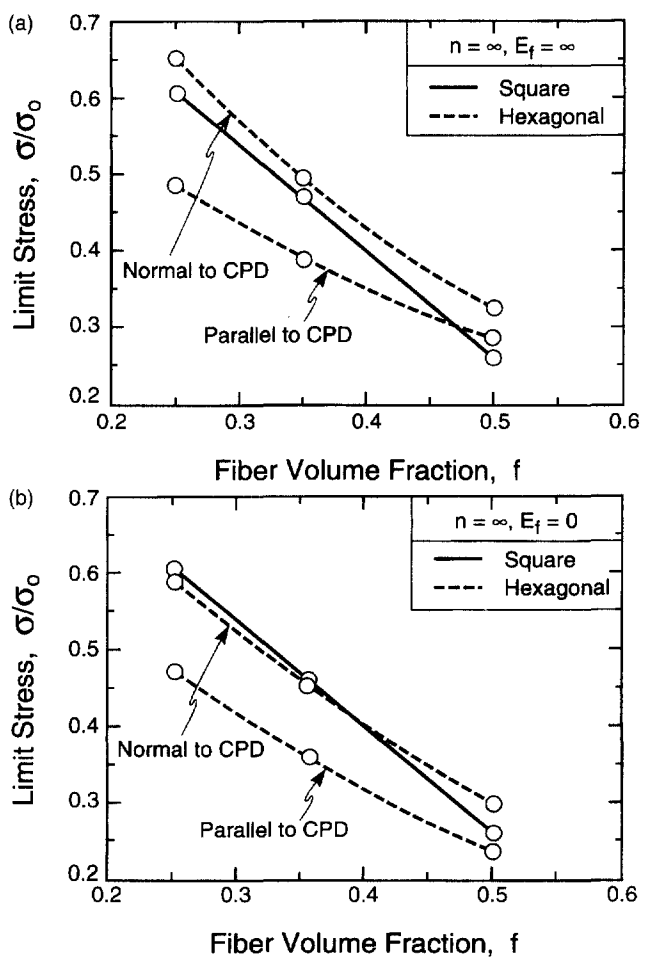

Fig. 3. Trends in the uniaxial limit stress with the fiber volume fraction for both hexagonal and square fiber arrangements, where the fibers are (a) rigid, or (b) perfectly compliant.

To gain further insight into the effects of the fiber modulus and the fiber arrangement on the flow response of the composite, the evolution of matrix plasticity within the composite has been calculated also. Figure 4(a) illustrates this behavior in a composite with rigid fibers in a hexagonal arrangement loaded normal to the CPD and a fiber volume fraction of 0.35. Figure 4(b) shows the corresponding results for a composite with perfectly compliant fibers. In both cases, plasticity initiates in the equatorial regions around the fibers. As the applied strain is increased, the plastic zone initially spreads in both the radial and hoop directions around the fibers. For the composite with perfectly compliant fibers, the plasticity subsequently spreads along the ligament joining nearest-neighbor fibers, at an angle of $\sim 30°$ to the loading direction. Once this ligament is completely yielded, the limit stress is attained. In the composite with rigid fibers, the plasticity initially spreads in a similar manner. However, the additional constraint associated with the fiber causes the plasticity to spread also in the direction normal to the loading axis, ultimately forming two plastic ligaments: one at 30° and the other at 90° to the loading axis. The same trends in

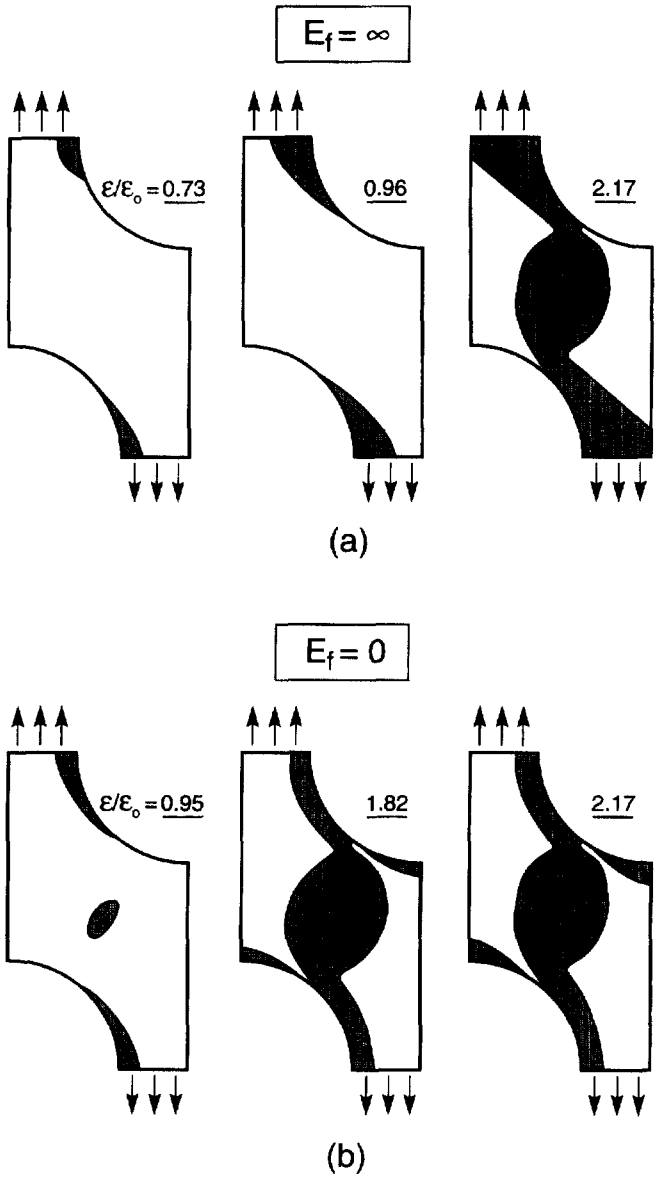

Fig. 4. Evolution of matrix plasticity (indicated by shaded regions) with applied strain, for (a), (b) hexagonal arrays loaded normal to the CPD, (c) hexagonal array loaded parallel to the CPD, and (d) square array. In all cases, the fiber volume fraction is 0.35.

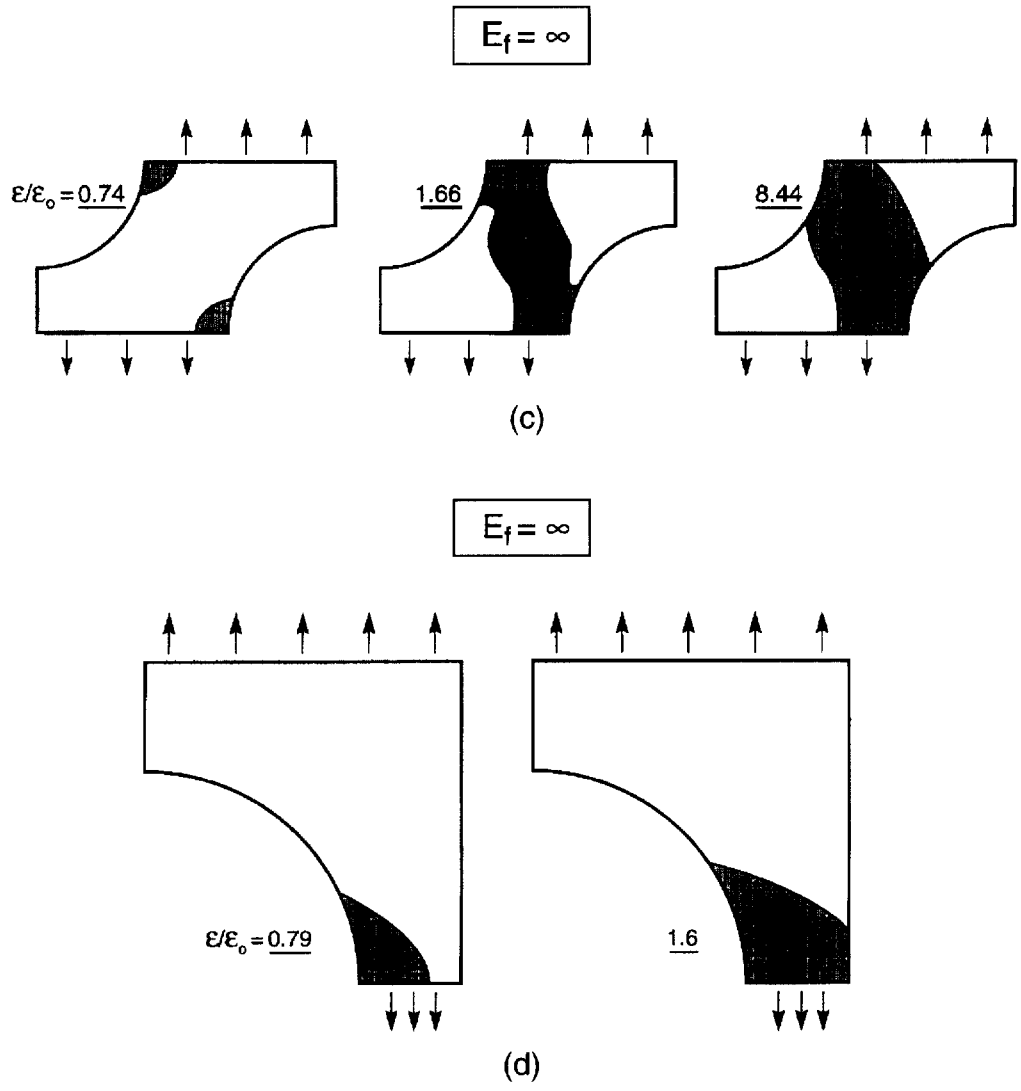

Fig. 4.—*Continued.*

the evolution of the plasticity were obtained for the other fiber volume fractions, $f = 0.25$ and 0.5. For the composites loaded parallel to the CPD, similar trends were again observed, with the exception that the plasticity remains confined to the ligaments between nearest-neighbor fibers, at 60° to the loading direction (Fig. 4(c)); it does not spread extensively along the plane normal to the loading direction.

Typical results for the square fiber arrangements are shown in Fig. 4(d). The plasticity again initiates in the equatorial regions around the fibers. For the high volume fractions, $f = 0.35$ and 0.5, it subsequently spreads normal to the loading direction, forming a plastic ligament between adjacent fibers. Essentially identical behavior is obtained for both rigid and perfectly compliant fibers, in accord with the strong similarities in the limit stress presented in Fig. 2(c). For the lowest volume fraction, $f = 0.25$, the plasticity initially spreads along the normal plane in a similar fashion. However, as the tip of this plastic zone approaches the cell boundary, a plastic zone develops and spreads along the cell diagonal (at $\sim 45°$ to the loading direction). Plastic failure ultimately occurs along this inclined plane.

In a subsequent section, an analytical model of net-section yielding is developed, based upon the assumption that the stresses are uniformly distributed along the potential failure planes. To assess the validity of this assumption, the distributions in stress have been

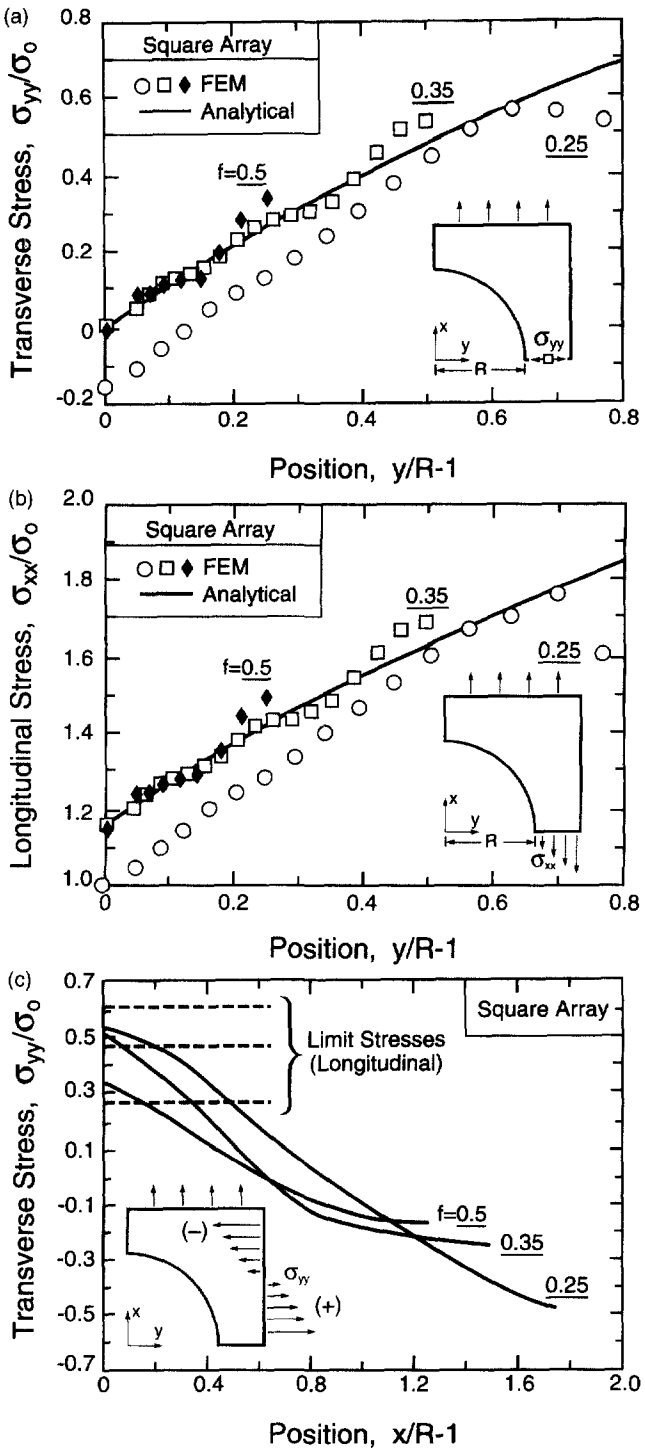

Fig. 5. Distributions of (a) transverse and (b) longitudinal stresses along the failure plane ($x = 0$), and (c) transverse stress along the cell boundaries ($y = W$).

calculated using FEM. Some representative results for the square fiber array with $E_f = \infty$ are shown in Fig. 5. For the two highest volume fractions, $f = 0.35$ and 0.5, the matrix separates from the fibers along the equatorial plane ($x = 0$) and, consequently, the transverse stress, σ_{yy}, in the matrix at this point is zero and the longitudinal stress is equivalent to the plane strain flow stress, $(2/\sqrt{3})\sigma_0$. However, at positions away from the interface along the plane $x = 0$, the transverse stress is tensile, increasing approximately linearly with

position, y/R. In order for the effective stress to remain at the flow stress, the corresponding longitudinal stress σ_{xx} along this plane follows a similar increasing trend with y/R. Similar results are obtained for both $f = 0.35$ and 0.5. For $f = 0.25$, the interface along the equatorial plane remains intact at the limit stress. At this point, the transverse stress in the matrix is compressive ($\sim -0.15\sigma_0$) and thus the longitudinal stress is below the plane strain flow stress: $\sim(2\sqrt{3}-0.15)\sigma_0 \approx \sigma_0$. However, both σ_{xx} and σ_{yy} increase with the distance, y/R, in essentially the same way as they do for the higher volume fractions. One notable exception is the slight decay in σ_{xx} and σ_{yy} at positions close to the cell boundary ($y/R \approx 1.8$). This decay is associated with the small elastic region along this plane. As noted earlier, plastic failure ultimately occurs along an inclined plane, at $\sim 45^\circ$ to the loading direction, not along the $x = 0$ plane.

The separation of the interfaces at the two highest fiber volume fractions and the stress gradients along the $x = 0$ plane are associated with the imposed boundary conditions along the cell edges, $y = W$. Had this boundary been allowed to remain traction-free, the matrix would have contracted laterally near the equatorial plane due to the yielding. The imposed condition that the cell boundary remain planar results in the development of transverse tensile stresses near the equatorial plane. However, since the average normal traction on this boundary must be zero, balancing compressive stresses are developed at other points on the boundary. Examples of these stress distributions for the square fiber arrays are shown on Fig. 5(c). It is of interest to note that the peak values of the transverse tension are comparable to the corresponding values of the longitudinal limit stress, indicating a rather high degree of stress triaxiality.

For the hexagonal fiber arrays, the stress distributions are somewhat different. When the load is parallel to the CPD, the stresses remain relatively uniform along the failure plane (at $\sim 60^\circ$ to the loading direction). This behavior is shown by the contour maps of σ_{xx} and σ_{xy} in Fig. 6. The results obtained for the hexagonal array loaded normal to the CPD were similar to those for the square array with the lowest fiber volume fraction. Notably, stress gradients were present along the yielded portion of the normal plane (A), though failure ultimately occurred on the inclined plane (B). The stresses along the failure plane were relatively uniform, as for the case where the load is applied parallel to the CPD.

Limited numerical studies have also been conducted for composites with a strain-hardening matrix. Figure 7(a) shows the effects of the hardening exponent, n, on the stress–strain curves for composites with rigid fibers in a hexagonal arrangement loaded normal to the CPD. In this case, the flow stress of the composite, $\sigma_c(\varepsilon)$, is normalized by the flow stress of the matrix alone, $\sigma_m(\varepsilon)$, at the same applied strain. The strength ratio, $\sigma_c(\varepsilon)/\sigma_m(\varepsilon)$, asymptotically approaches a constant value at strains of the order $\varepsilon/\varepsilon_0 \gtrsim 20$–$50$. The asymptotic values of the strength ratio are plotted against the hardening exponent in Fig. 7(b) for composites with three different fiber volume fractions. Evidently the asymptotic stress ratio is very insensitive to n when the fibers are perfectly compliant and essentially independent of n when the fibers are rigid. Moreover, the differences between perfectly compliant and rigid fibers decrease with increasing n; for $n \geqslant 0.2$, the two limit stress ratios are within ~ 2–3% of one another.

The trends in the limiting strength ratio with the hardening exponent differ from the results obtained for well-bonded fiber and particulate composites. In the well-bonded systems, the limiting strength ratio increases substantially with n; for example, in the case of spherical particulate reinforcements, it increases from 1.28 to 1.67 as n is increased from 0 to 0.2 (Brockenbrough and Zok, 1995). Similar increases are obtained in the well-bonded fiber-reinforced systems (Zahl *et al.*, 1994). Moreover, the magnitude of the strains required to obtain the limiting strength are very much higher in the composites with weakly bonded interfaces. Typically, in the well-bonded systems, the asymptotic level is reached within $\varepsilon/\varepsilon_0 \sim 2$–$5$ (depending on f and n): about an order of magnitude smaller than the values obtained for the weakly-bonded systems.

3.2. *Biaxial tension*

A series of FEM calculations were performed for biaxial loading of the square and hexagonal fiber arrays with $f = 0.35$. The limiting values of the two stress components are

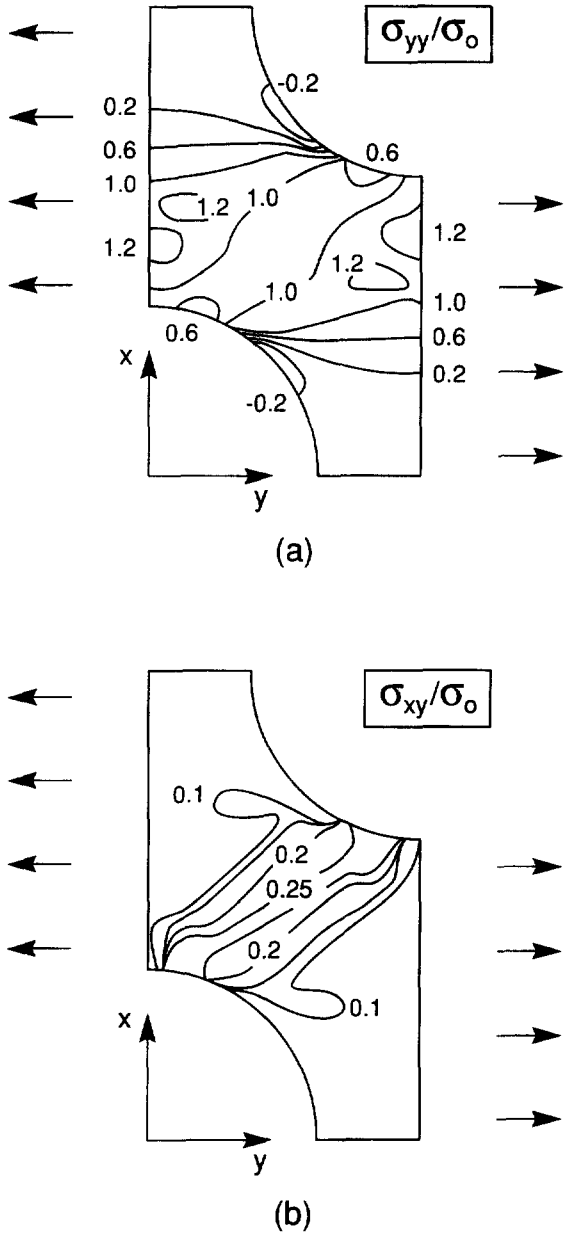

Fig. 6. Contour maps showing distributions in the longitudinal and shear stresses, σ_{yy} and σ_{xy} for a hexagonal fiber array loaded parallel to the CPD. Note the uniformity in these stresses across the ligament joining the two fibers.

plotted in Fig. 8. Also shown for comparison is the yield surface for a monolithic metal under plane strain loading conditions, given by

$$\sigma_{xx} - \sigma_{yy} = \pm \frac{2\sqrt{3}}{3}\sigma_0 \tag{2}$$

For the square array, the composite yield surface is symmetric about the line $\sigma_{xx} = \sigma_{yy}$ because of the symmetry of the cell. In the regime $\sigma_{xx}, \sigma_{yy} > 0$, yielding occurs when either σ_{xx} or σ_{yy} reaches a critical value, $\sim 0.46\sigma_0$, independent of the other stress component. As the stresses become negative, the shape of the yield surface changes. In the limit wherein both σ_{xx} and σ_{yy} are $\ll 0$, the yield surface approaches that of the monolithic metal [given

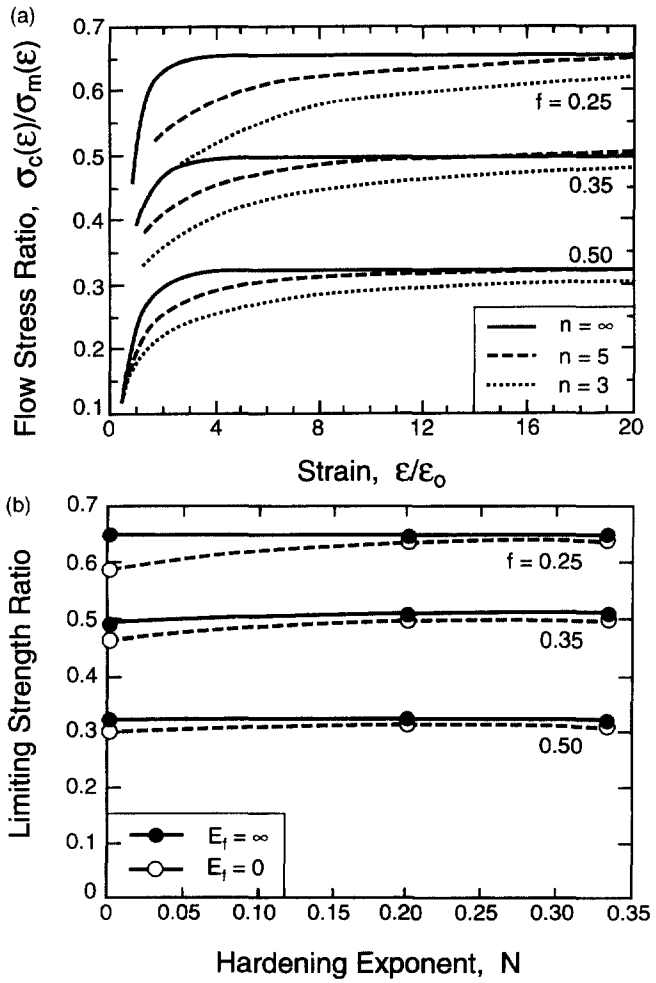

Fig. 7. Effects of the matrix hardening exponent on (a) the stress–strain response and (b) and asymptotic strength ratio, for composites with rigid fibers in a hexagonal array loaded normal to the CPD. The stresses are normalized by the flow stress of the matrix alone at the same applied strain.

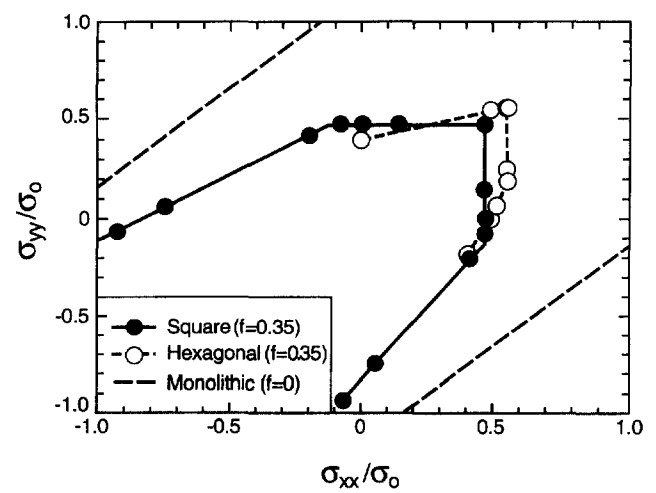

Fig. 8. Limit stresses for biaxial loading of both square and hexagonal fiber arrays.

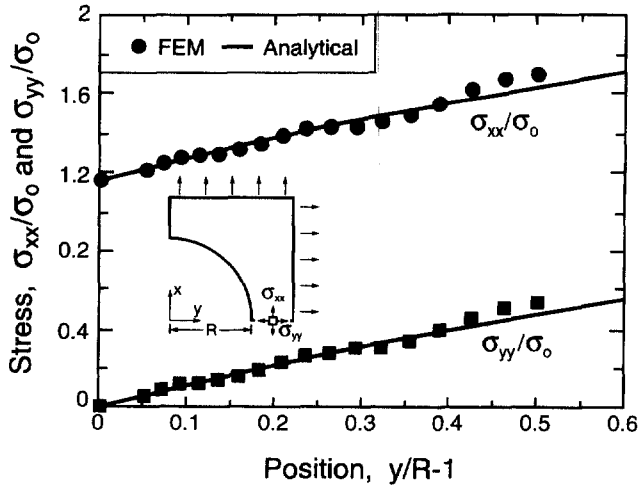

Fig. 9. Stress distributions along failure plane ($x = 0$) for uniform biaxial tensile loading of a square fiber array with $f = 0.35$. Also shown for comparison are the predictions based on the uniform expansion of a cylinder [eqns (17) and (18)].

by eqn (2)]. In this limit, similar results would be expected for well-bonded fiber composites. Yield surfaces with similar shapes have been developed for the compaction of an array of plastic cylinders, though the stresses are compressive and the cell geometry is different (Akisanya and Cocks, 1995).

The yield surface for the hexagonal array exhibits several slightly different features. (i) It is not symmetric about $\sigma_{xx} = \sigma_{yy}$. (ii) The composite is somewhat stronger in the x-direction (normal to the CPD) than in the y-direction. (iii) There is only a small portion of the yield surface that does not depend on both stress components (top right corner of Fig. 8).

Figure 9 shows the stress distribution along the failure plane in the square array for uniform biaxial tensile loading. Evidently the distributions are almost identical to those obtained for uniaxial loading (compare with Figs 5(a) and (b)). These similarities can be rationalized in terms of the transverse stresses that develop under uniaxial loading, as described previously. These similarities are manifested in the insensitivity of the limiting values of one of the applied stresses, σ_{xx}, to the other, σ_{yy}, as seen in Fig. 8.

4. NET-SECTION YIELDING MODEL

4.1. *Uniaxial tension*

The FEM calculations show that the limit stresses are insensitive to the modulus of the fibers. For fiber volume fractions typical of most Ti/SiC composites, $f \sim 0.35$, the difference in strengths between the rigid fibers and the perfectly compliant ones is negligible for the square fiber array and only ~6–7% for the hexagonal arrays. The results indicate that the composite behaves essentially the same as a matrix containing an array of holes. This result, in turn, suggests that the limit stress may be calculated on the basis of net-section yielding, neglecting the contributions from the fibers. Such an approach is developed here.

The situation in which the fibers are in a hexagonal array and loaded normal to the CPD is considered first (Fig. 1(c)). From the geometry, the cell height, H, and the cell width, L, are related to the fiber volume fraction, f, and the fiber radius, R, through the relations

$$\frac{H}{2R} = \sqrt{\frac{\sqrt{3}}{8}\frac{\pi}{f}} \tag{3}$$

and

$$\frac{L}{2R} = \sqrt{\frac{\sqrt{3}}{24}\frac{\pi}{f}} \tag{4}$$

In this configuration, plasticity tends to develop along one of two planes: the first at $\sim 30^\circ$ to the loading direction (B in Fig. 1(c)), and the other along the equatorial plane normal to the loading direction (A). The limit strength of the composite is then expected to be the lower of the stress levels required to cause yielding along these two planes. In calculating the critical stress levels, it is assumed initially that the stresses are distributed uniformly along each of the two planes, with no stress or strain concentrations arising from the holes.

Across plane B, both a normal tensile stress, σ_B, and a shear stress, τ_B, are present. The relations between these stresses and the applied stress, σ_{xx}^{∞}, are obtained from equilibrium considerations. The relations are

$$\frac{\tau_B}{\sigma_B} = \frac{\cos(\pi/6)}{\cos(\pi/3)} = \sqrt{3} \tag{5}$$

and

$$\sigma_{xx}\sqrt{\frac{\sqrt{3}}{24}\frac{\pi}{f}} = \frac{\tau_B\sqrt{3}}{2}\left[\sqrt{\frac{\sqrt{3}}{6}\frac{\pi}{f}} - 1\right] + \frac{\sigma_B}{2}\left[\sqrt{\frac{\sqrt{3}}{6}\frac{\pi}{f}} - 1\right] \tag{6}$$

Under plane strain conditions, the effective (Mises) stress, $\bar{\sigma}_B$, corresponding to these two stresses is [10]:

$$\bar{\sigma}_B = \sqrt{\tfrac{3}{4}\sigma_B^2 + 3\tau_B^2} \tag{7}$$

Yielding occurs when $\bar{\sigma}_B = \sigma_0$. Combining eqns (5)–(7) with the yield criterion gives the limiting value of the remote stress, σ_{xx}^l:

$$\frac{\sigma_{xx}^l}{\sigma_0} = \frac{8}{\sqrt{39}}\left[1 - \sqrt{2\sqrt{3}\frac{f}{\pi}}\right] \tag{8}$$

Plane A is subjected only to a tensile stress, σ_A, given by

$$\frac{\sigma_A}{\sigma_{xx}} = \left[1 - \sqrt{\frac{2\sqrt{3}f}{\pi}}\right]^{-1} \tag{9}$$

The effective stress on this plane is

$$\bar{\sigma}_A = \frac{\sqrt{3}}{2}\sigma_A \tag{10}$$

Combining eqns (9) and (10) with the yield criterion gives the limiting stress as:

$$\frac{\sigma_{xx}^l}{\sigma_0} = \frac{2}{\sqrt{3}}\left[1 - \sqrt{2\sqrt{3}\frac{f}{\pi}}\right] \tag{11}$$

Comparison of eqns (8) and (11) shows that the limit stress predicted by eqn (11) is always the lower of the two; the ratio of the stresses is $4/\sqrt{13} \approx 1.11$.

The same approach is used to evaluate the limit stresses for hexagonal fiber arrays loaded parallel to the CPD (along the y-direction). The two potential failure planes are B and C. The limit stresses for yielding along these two planes are

$$\frac{\sigma'_{yy}}{\sigma_0} = \frac{8\sqrt{7}}{21}\left[1-\sqrt{2\sqrt{3}\frac{f}{\pi}}\right] \quad \text{(Plane B)} \tag{12}$$

and

$$\frac{\sigma'_{yy}}{\sigma_0} = \frac{2\sqrt{3}}{3}\left[1-\sqrt{\frac{2\sqrt{3}}{3}\frac{f}{\pi}}\right] \quad \text{(Plane C)} \tag{13}$$

The value predicted by eqn (12) is always the lower of the two.

For the square fiber array, the cell dimension, W, is related to R and f through

$$\frac{W}{2R} = \frac{1}{4}\sqrt{\frac{\pi}{f}} \tag{14}$$

The limit stresses are

$$\frac{\sigma'_{xx}}{\sigma_0} = \frac{\sigma'_{yy}}{\sigma_0} = \frac{4\sqrt{15}}{15}\left[1-\sqrt{\frac{2f}{\pi}}\right] \quad \text{(Plane E)} \tag{15}$$

and

$$\frac{\sigma'_{xx}}{\sigma_0} = \frac{\sigma'_{yy}}{\sigma_0} = \frac{2\sqrt{3}}{3}\left[1-2\sqrt{\frac{f}{\pi}}\right] \quad \text{(Planes D and F)} \tag{16}$$

where sections D, E and F are indicated on Fig. 1(d). Equation (16) predicts the lower of the two limit stress for all values of f.

The limit stresses predicted by eqns (8), (11)–(13), (15) and (16) are plotted as a function of fiber volume fraction in Fig. 10. (These predictions are labeled as "Simple Net-Section Model" to distinguish them from the modified version which is described below.) For comparison, the results obtained from the FEM calculations are also shown.

For the hexagonal array loaded parallel to the CPD (Fig. 10(a)), the net-section prediction is in excellent agreement with the FEM results: the differences being $<2\%$ for both $f = 0.25$ and 0.35 and $\sim 9\%$ for $f = 0.5$. The net-section model also correctly predicts that plastic failure should occur along the inclined plane, B. These correlations are consistent with the uniformity in the stresses across this plane, shown in Fig. 6.

For the hexagonal array loaded normal to the CPD (Fig. 10(b)), the net-section model predicts failure along plane A; in contrast, the FEM results indicate that it occurs along plane B at a somewhat higher stress. This discrepancy appears to be associated with the stress gradients along plane A, leading both to an elevation in the flow stress and a transition in the failure plane from A to B. Indeed, the net-section predictions for plane B are in very good agreement with the FEM results. (The effects of the stress gradients on the limit stress for plane A are presented later.)

For the square array, the net-section model predicts failure along the normal planes, D or F, depending on whether the load is applied in the x- or y-directions. The FEM results indicate that, for $f = 0.35$ and 0.5, failure does indeed occur along these planes, though at stress levels that are higher than the net-section predictions. The FEM results also indicate, that for $f = 0.25$, failure occurs along the inclined plane, E, rather than D or F. The net-section prediction for plane E at this volume fraction is in good agreement with the FEM result.

The stress gradients acting along the planes normal to the loading direction have previously been analyzed for the case of a rectangular bar containing a circular hole of radius, R, subject to uniaxial tensile loading (Hill, 1989; Kaliszky, 1989). In this case, the slip-line field around the hole consists of a series of logarithmic spirals. Within the plastic zone, the stresses acting across the plane of minimum cross section are

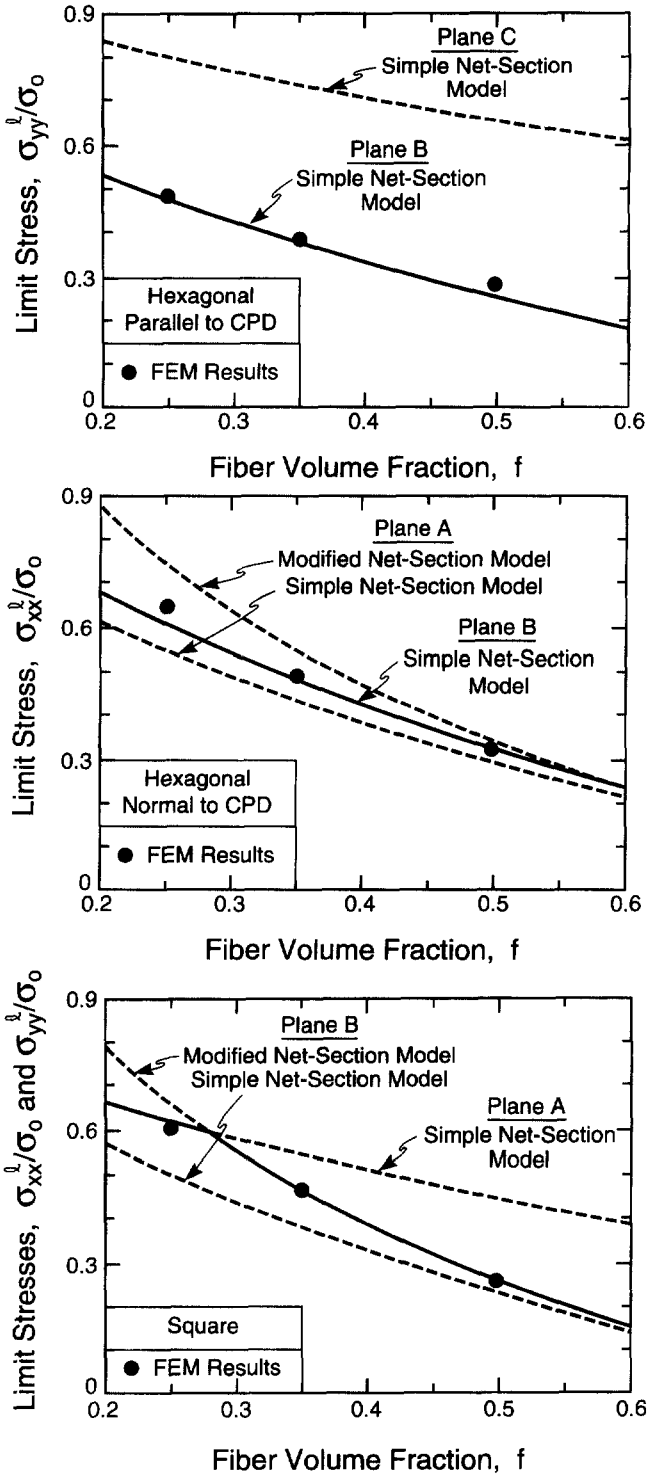

Fig. 10. Comparisons of analytical predictions of limit stresses for uniaxial loading with those obtained using FEM.

$$\frac{\sigma_{yy}}{\sigma_0} = \frac{2\sqrt{3}}{3}\ln(r/R) \tag{17}$$

and

$$\frac{\sigma_{xx}}{\sigma_0} = \frac{2\sqrt{3}}{3}(1+\ln r/R) \tag{18}$$

where r is the radial distance measured from the center of the hole and x represents the direction of loading. Figure 5 shows comparisons between these predictions and the ones obtained from the FEM calculations for the square fiber array subject to uniaxial loading. Good correlations are obtained for the two highest volume fractions. For the lowest volume fraction, the two follow similar increasing trends with y/R, though the analytical results are somewhat higher than the numerical ones. This discrepancy is due to the contact of the matrix with the fiber along the equatorial plane and the resulting compressive stress acting normal to the interface.

The solutions for the stress gradients can be used to modify the predicted limit stresses. This is accomplished by multiplying the results in eqns (11) and (15) by a numerical coefficient, λ, defined by the ratio of the average normal stress, $\hat{\sigma}$, acting along the failure plane perpendicular to the loading direction (obtained from the slip-line solution) to the plane strain yield stress, $(2\sqrt{3}/3)\sigma_0$. In general, λ is given by

$$\lambda \equiv \frac{\sqrt{3}\hat{\sigma}}{2\sigma_0} = \frac{\sqrt{3}}{2(r_0 - R)\sigma_0}\int_R^{r_0} \sigma_{\theta\theta}(r)\,\mathrm{d}r \tag{19}$$

where r_0 is the limiting distance, taken as W for the square array, and either H or L for the hexagonal array depending on the loading direction. λ is obtained by substituting eqn (17) into (19) along with the appropriate value of r_0, and then combining the result with the relationship between the cell dimensions and the fiber volume fraction (either eqns (3), (4) or (14)). For the square array, the result is:

$$\lambda = \frac{\ln\left(\dfrac{W}{R}\right)}{1 - \dfrac{R}{W}} = \frac{\ln\left(\dfrac{1}{2}\sqrt{\dfrac{\pi}{f}}\right)}{1 - 2\sqrt{\dfrac{f}{\pi}}} \tag{20}$$

For the hexagonal array loaded normal to the CPD, it is

$$\lambda = \frac{\ln\left(\dfrac{L}{R}\right)}{1 - \dfrac{R}{L}} = \frac{\ln\left(\sqrt{\dfrac{\sqrt{3}\pi}{6f}}\right)}{1 - \sqrt{\dfrac{2\sqrt{3}f}{\pi}}} \tag{21}$$

and for the hexagonal array loaded parallel to the CPD, it is

$$\lambda = \frac{\ln\sqrt{\dfrac{\sqrt{3}\pi}{2f}}}{1 - \sqrt{\dfrac{2\sqrt{3}f}{3\pi}}} \tag{22}$$

Figures 10(b) and (c) show the predictions obtained from the modified versions of the net-section yielding model (incorporating the stress gradients). The solutions are obtained by multiplying the right side of eqn (15) by λ in eqn (20), and multiplying the right side of eqn (11) by λ in eqn (21). For the hexagonal array (Fig. 10(b)), the modified model predicts a limit stress for plane A which is higher than that needed for yielding along plane B, in accord with the FEM prediction that failure occurs on plane B. For the square array, the modified model yields predictions for yielding along plane E that are in excellent agreement with the FEM results for volume fractions at which failure does indeed occur along E ($f = 0.35$ and 0.5); for $f = 0.25$, it predicts a limit stress for E that exceeds that for planes

D or F and thus correctly predicts the transition in the failure planes as the fiber volume fraction is reduced.

4.2. *Biaxial loading*

The net-section yielding model has been extended to calculate the limiting yield surface of the composite under biaxial tensile loading. For this purpose, two stress parameters are introduced: a mean stress, σ_m, and a deviatoric stress, $\Delta\sigma$, defined by

$$\sigma_m \equiv (\sigma_{xx}+\sigma_{yy})/2 \tag{23}$$

and

$$\Delta\sigma \equiv (\sigma_{xx}-\sigma_{yy})/2 \tag{24}$$

where σ_{xx} and σ_{yy} are the stresses applied along the directions indicated in Fig. 1. These parameters have been used previously by others to describe the yield surfaces for porous materials (Akisanya and Cocks, 1995; Sofronis and McMeeking, 1992). The combinations of $\Delta\sigma$ and σ_m that lead to plastic collapse are calculated using the approach outlined above. Notably, the potential critical planes are identified, the average normal and shear stresses acting along each of these planes are evaluated and the stresses then combined with the Mises yield criterion. For planes oriented normal to either the x- or y-directions, the factor, λ, is also incorporated. (It can be shown readily that the stress gradients that occur around a cylindrical hole under uniform biaxial tension are identical to the ones described by eqns (17) and (18) for uniaxial tension, with σ_{yy} replaced by the hoop stress, $\sigma_{\theta\theta}$, and σ_{xx} replaced by the radial stress, σ_{rr}. Consequently λ is expected to be independent of the imposed stress state.) The limit surface is obtained from the inner envelope of the yield surfaces calculated for all planes.

For the square fiber array, yielding can occur on planes D, E or F (Fig. 1(d)). The normal and shear stresses on plane E are

$$\sigma_E = \frac{\sigma_{xx}+\sigma_{yy}}{2(1-\sqrt{2f/\pi})} = \frac{\sigma_m}{1-\sqrt{2f/\pi}} \tag{25}$$

and

$$\tau_E = \frac{\sigma_{xx}-\sigma_{yy}}{2(1-\sqrt{2f/\pi})} = \frac{\Delta\sigma}{(1-\sqrt{2f/\pi})} \tag{26}$$

and the corresponding yield condition is

$$\left(\frac{\sigma_m}{\sigma_0}\right)^2 + \left(\frac{2\Delta\sigma}{\sigma_0}\right)^2 = \frac{4}{3}(1-2\sqrt{f/\pi})^2 \tag{27}$$

Planes D and F are subjected only to normal stresses, given by

$$\sigma_D = \frac{\sigma_m+\Delta\sigma}{1-2\sqrt{f/\pi}} \tag{28}$$

and

$$\sigma_F = \frac{\sigma_m-\Delta\sigma}{1-2\sqrt{f/\pi}} \tag{29}$$

The yield conditions are

$$\frac{\sigma_m}{\sigma_0} + \frac{\Delta\sigma}{\sigma_0} = \pm\frac{2\sqrt{3}}{3}\lambda[1-2\sqrt{f/\pi}] \quad \text{(Plane D)} \tag{30}$$

and

$$\frac{\sigma_m}{\sigma_0} - \frac{\Delta\sigma}{\sigma_0} = \pm\frac{2\sqrt{3}}{3}\lambda[1-2\sqrt{f/\pi}] \quad \text{(Plane F)} \tag{31}$$

Equations (27), (30) and (31) are plotted in Fig. 11(a) for a fiber volume fraction, $f = 0.35$. The inner surface along which yielding is predicted to occur is indicated by the shading. The FEM results are also shown in this figure.

Since the model neglects the contributions from the fibers, it is expected to be valid only when both σ_{xx} and σ_{yy} are positive. This condition can be written in terms of the two stress parameters as

$$-\sigma_m \leqslant \Delta\sigma \leqslant \sigma_m \tag{32}$$

This result is plotted on Fig. 11 as two dotted lines. Within this regime, yield occurs on planes D or F, depending on whether $\Delta\sigma$ is negative or positive; the stresses required for

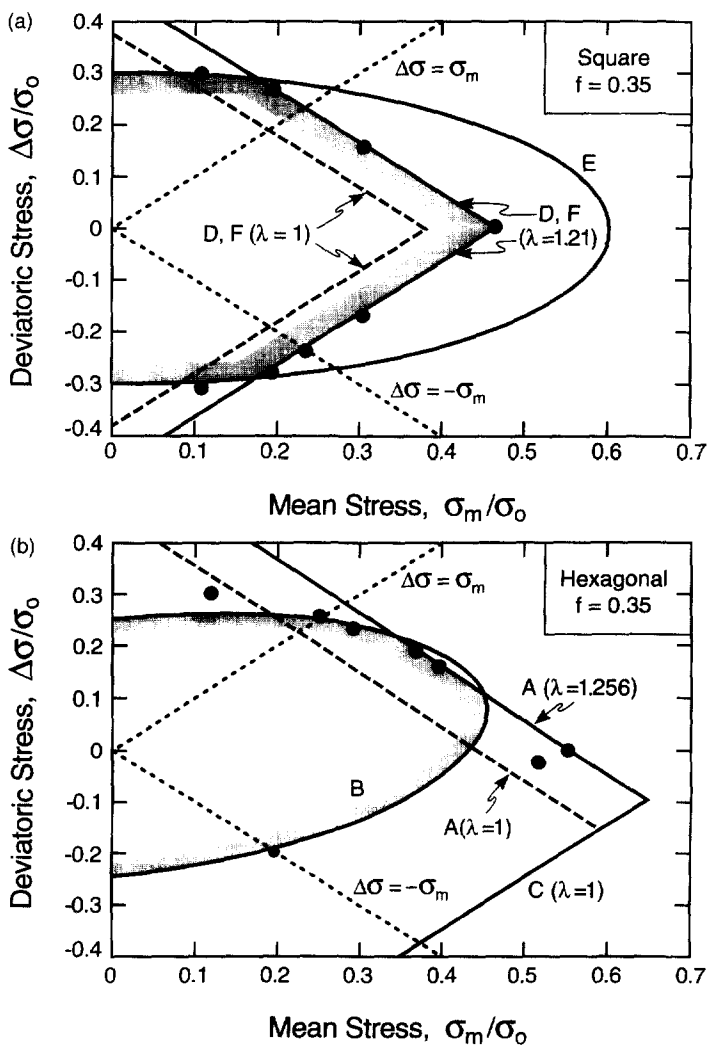

Fig. 11. Limiting yield surfaces for composites with $f = 0.35$: (a) square and (b) hexagonal fiber arrays.

yielding on plane E are always higher and thus are not attained. Yielding on plane E is predicted to occur when

$$\sigma_m/\sigma_0 \lesssim 0.18 \tag{33}$$

Despite the fact that this range is outside of the one defined by eqn (32), the predictions remain in good agreement with the FEM results, suggesting that the model is accurate even when one of the stress components is somewhat negative. It should be noted also that, because of the symmetry of the unit cell, the yield surface is symmetric about the line $\Delta\sigma = 0$.

As noted earlier, the yield surface becomes insensitive to σ_m when $\sigma_m/\sigma_0 \ll 0$. In this limit, the yield surface is expected to be essentially the same as that of a well-bonded fiber composite neglecting the differences associated with sliding vs non-sliding interfaces. Yield is then predicted to occur when $|2\Delta\sigma|$ reaches the plane strain flow stress of the matrix, $(2/\sqrt{3})\sigma_0$, such that

$$\left|\frac{\Delta\sigma}{\sigma_0}\right| = 1/\sqrt{3} = 0.577 \tag{34}$$

Following the same approach, the limit surfaces for the hexagonal fiber arrays have been obtained. The relevant results are

$$\frac{\sigma_m}{\sigma_0} + \frac{\Delta\sigma}{\sigma_0} = \pm\frac{2\sqrt{3}}{3}\lambda(1-\sqrt{2\sqrt{3}f/\pi}) \tag{35}$$

for plane A;

$$\left(\frac{\sigma_m}{\sigma_0} - \frac{\Delta\sigma}{2\sigma_0}\right)^2 + 3\left(\frac{\Delta\sigma}{\sigma_0}\right)^2 = \frac{4}{3}(1-\sqrt{2\sqrt{3}f/\pi})^2 \tag{36}$$

for plane B; and

$$\frac{\sigma_m}{\sigma_0} - \frac{\Delta\sigma}{\sigma_0} = \pm\frac{2\sqrt{3}}{3}\lambda(1-\sqrt{2f/\sqrt{3}\pi}) \tag{37}$$

for plane C.

The yield surfaces for $f = 0.35$ are plotted in Fig. 11(b), along with the FEM results and the lines defined by eqn (32). For this fiber array, the axes that define the symmetry of the cell are different from those defining the principal stresses; consequently, the yield surfaces are not symmetric about $\Delta\sigma = 0$. The analytical results predict failure along plane B for most stress combinations, the exception being the region in the top right corner of the yield surface where failure occurs along plane A. The agreement between the analytical and numerical results is good for cases where $\Delta\sigma/\sigma_0$ is not zero. When it is zero (i.e. uniform biaxial tension), the analytical result for yielding along plane B is $\sim 20\%$ less than the numerical one. This discrepancy arises because, under uniform biaxial loading, stress gradients develop along plane B; indeed, in this limit, they are identical to those along plane A. As a result, the limit stress is underestimated. The more relevant result in this limit is the one for yielding along plane A, incorporating the effects of stress gradients. In this case, the analytical result is essentially identical to the numerical one. In its present form, the net-section yielding model does not take into account changes in stress gradients with stress state: the gradients are either neglected altogether (as they should for yielding along inclined planes under near-uniaxial loading) or are included for all stress states (for planes oriented normal to the principal loading directions). The shear stresses acting along the

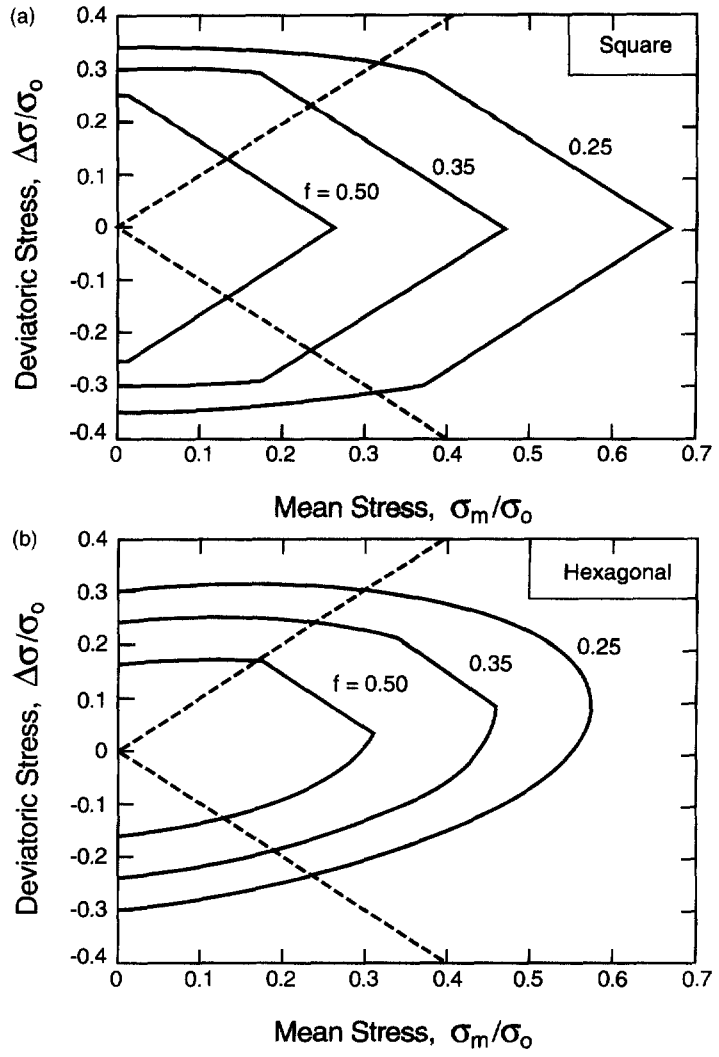

Fig. 12. Effects of fiber volume fraction on the yield surfaces for (a) square and (b) hexagonal fiber arrays.

inclined planes effectively eliminate the stress gradients. However, under uniform biaxial loading, these shear stresses vanish and the stress gradients become important.

The effects of fiber volume fraction on the yield surfaces for both types of fiber arrays are shown in Fig. 12. In these cases, only the inner yield surfaces from the analytical solutions are shown. The yield surfaces for the various volume fractions nest inside one another, expanding as f decreases. In the limit of $f \to 0$, the yield surface approaches that of a monolithic metal under plane strain conditions. It should be emphasized that the accuracy of the yield surfaces that lie outside the range $-\sigma_m \leqslant \sigma \leqslant \sigma_m$ may be questionable in some cases. Furthermore, for the hexagonal arrays, the predictions along $\Delta\sigma/\sigma_0 \approx 0$ are expected to be lower bounds to the actual limiting stresses.

5. CONCLUDING REMARKS

The limit stresses for biaxial loading of weakly-bonded unidirectional fiber composites have been evaluated and used to construct limit surfaces in an appropriate stress space. The limit stresses depend somewhat on the fiber array as well as the directions of loading but are insensitive to the fiber modulus. The limiting conditions are obtained when plastic failure occurs along the most favorably oriented plane within the matrix. Transitions in the failure plane can occur with changes in the fiber volume fraction or imposed stress state.

Such effects can be accurately described through the use of a net-section yielding model, incorporating the stress gradients that occur along planes oriented perpendicular to the principal loading directions. The attractive features of the net-section yielding model include its simplicity as well as the potential for extending it to other situations, including other fiber volume fractions and fiber arrangements, without recourse to the numerical calculations.

Acknowledgements—Funding for this work was supplied by the DARPA University Research Initiative Program at UCSB under ONR contract N0014-92-J-1808. Fruitful discussions with R. M. McMeeking are gratefully acknowledged. The ABAQUS finite element code was made available by Hibbitt, Karlsson and Sorensen, Inc., Pawtucket, RI, through an academic license.

REFERENCES

ABAQUS User Manual (1994) Hibbitt, Karlsson and Sorensen, Inc., 1080 Main Street, Pawtucket, RI.

Akisanya, A. R. and Cocks, A. C. F. (1995) Stage I compaction of cylindrical particles under non-hydrostatic loading. *Journal of the Mechanics and Physics of Solids* **43,** 605–636.

Böhm, H. J. and Rammerstorfer (1991) Micromechanical investigation of the processing and loading of fiber-reinforced metal matrix composites. *Materials Science and Engineering* **A135,** 185–188.

Brockenbrough, J. R. and Suresh, S. (1990) Plastic deformation of continuous fiber-reinforced metal matrix composites: effects of fiber shape and distribution. *Scripta Metallurgica et Materialia* **24,** 325–330.

Brockenbrough, J. R., Suresh, S. and Wienecke, H. A. (1991) Deformation of metal-matrix composites with continuous fibers: geometrical effects of fiber distribution and shape. *Acta Metallurgica et Materialia* **39,** 735–752.

Brockenbrough, J. A. and Zok, F. W. (1995) On the role of particle cracking in flow and fracture of metal matrix composites. *Acta Metallurgica et Materialia* **43,** 11–20.

Du, Z.-Z. and McMeeking, R. M. (1994) Control of strength anisotropy of metal matrix fiber composites. *Journal of Computer-Aided Materials Design* **1,** 243–264.

Du, Z.-Z., Leckie, F. A. and Burr, A. (1996) Design with titanium matrix composites: case studies, in preparation.

Gunawardena, S. R., Jansson, S. and Leckie, F. A. (1993) Modeling of anisotropic behavior of weakly bonded fiber reinforced MMCs. *Acta Metallurgica et Materialia* **41,** 3147–3156.

Hill, R. (1989) *The Mathematical Theory of Plasticity*. Clarendon Press, Oxford, pp. 245–252.

Jansson, S. and Leckie, F. A. (1992) Mechanical behaviour of a continuous fiber-reinforced aluminum matrix composite subjected to transverse and thermal loading. *Journal of the Mechanics and Physics of Solids* **40,** 593–612.

Jansson, S., Dève, H. and Evans, A. G. (1991) The anisotropic mechanical properties of a Ti matrix composite reinforced with SiC fibers. *Metallurgical Transactions* **22A,** 2975–2984.

Jansson, S. and Leckie, F. A. (1994) Transverse tensile and inplane shear strength of weakly bonded fiber reinforced MMCs subjected to cyclic thermal loading. *Mechanics of Materials* **18,** 205–212.

Kaliszky, S. (1989) *Plasticity: Theory and Engineering Applications*. Elsevier, Amsterdam, pp. 205–208.

Nakamura, T. and Suresh, S. (1993) Effects of thermal residual stresses and fiber packing on deformation of metal matrix composites. *Acta Metallurgica et Materialia* **41,** 1665–1681.

Nimmer, R. P., Bankert, R. J., Russell, E. S., Smith, G. A. and Wright, P. K. (1991) Micromechanical modeling of fiber matrix interface effects in transversely loaded SiC/Ti-6-4 metal matrix composites. *Journal of Composites and Technological Research* **13,** 3–13.

Odqvist, F. K. G. (1966) *The Mathematical Theory of Creep and Creep Rupture*. Oxford University Press.

Sofronis, P. and McMeeking, R. M. (1992) Creep of power-law material containing spherical voids. *Transactions of ASME* **59,** S88–S95.

Teply, J. L. and Dvorak, G. J. (1988) Bounds on overall instantaneous properties of elastic-plastic composites, *Journal of the Mechanics and Physics of Solids* **36,** 29–58.

Weber, C. H., Du, Z.-Z. and Zok, F. W. (1996) High temperature deformation and fracture of a fiber reinforced titanium matrix composite. *Acta Metallurgica et Materialia* **44,** 683–695.

Zahl, D. B., Schmauder, S. and McMeeking, R. M. (1994) Transverse strength of metal matrix composites reinforced with strongly bonded continuous fibers in regular arrangements. *Acta Metallurgica et Materialia* **42,** 2983–2997.